Abstract

We report the characterisation of microstructures and high-cycle-fatigue (HCF) properties of Type 304 stainless steel joints processed by brazing. Pure copper was applied as the filler metal for brazing at 1120 °C. A two-phase microstructure was obtained within the joint region: the star-shaped precipitates and copper matrix. The precipitates with an average size of 0.43 μm were rich in iron and chromium. A fixed orientation relationship was found between the precipitates and copper matrix. The joint exhibited much higher tensile strength and HCF life when compared to pure copper. The strength enhancement can be attributed to the presence of precipitates. Furthermore, the effect of joint interface roughness as well as defects were critically investigated. The joint interface roughness showed little influence on the HCF lives. Post-examinations revealed that fatigue crack initiation and propagation occurred entirely within the joint region, hence being consistent with the similar HCF lives regardless of the pre-defined interface roughness conditions. In addition, it was found that the HCF lives decreased exponentially with the increase of initial defect area. Fractography analysis revealed that fatigue striation spacings near the crack initiation zone increased with the increase of defect area, suggesting that the larger defects result in higher crack growth rate, hence shorten the overall fatigue life.

1. Introduction

Copper and its alloys are usually adopted as the filler material for brazing of stainless steel (SS) components. In general, copper provides good wettability and minimises thermal distortion. This is because the coefficient of thermal expansion (CTE) of SS is approximately 17.0 $\times 10^{-6}$ K^{-1} [1], which is very close to that of pure copper, i.e., ~16.5$\times 10^{-6}$ K^{-1} [2]. As a consequence, a limited magnitude of thermal residual stress would be expected in the brazing assembly. There are many processing parameters that could affect the mechanical properties of brazed joints, such as joint gap width, brazing temperature, interface roughness and presence of joint defects. The two that concern us in the present work are (i) joint interface roughness and (ii) joint defect. The joint interface roughness is defined as the roughness conditions for the bonding surfaces of the base metal prior to brazing.

To date, no work has been undertaken to understand the effect of interface roughness on high-cycle-fatigue (HCF) strength in stainless steel brazed joints, although some studies were performed on other base metals. For instance, Kawakatsu and Suezawa [3] studied the effect of interface roughness on the fatigue properties of mild steel brazed joints. Hong and Koo [4] evaluated the influences of base metal roughness on the shear strength of Ti-6Al-4V brazed joints. Zaharinie et al. [5] investigated the impact of base metal roughness on the wetting behaviour of the filler materials for copper brazed joints. In addition, Suezawa [6] studied the effect of joint interface roughness on tensile and HCF strength in mild steel brazed joints where a silver-copper (Ag-Cu) eutectic alloy was used as the filler metal. A range of interface roughness conditions were created by using different P-Grade SiC papers from P60 to P600. The maximum tensile strength of 425 MPa and the corresponding HCF fatigue limit of 172 MPa (the stress amplitude that a material can withstand at 10^7 cycles without failure) were obtained for the mild steel brazed joint that had been prepared with P120. The P60 interface roughness exhibited a lower joint strength (both static and HCF) when compared to P120, but the underlying reason was not explored explicitly. This work suggested that a coarser joint interface led to a higher strength of the final brazed joint. This was qualitatively attributed to the enlarged bonding area of a coarser interface. However, this hypothesis deserves further experimental verification because all the brazed joints failed entirely within the joint region rather than the filler/base metal interface [6].

Zaharinie et al. [5] studied the effect of joint interface roughness on the microstructure of pure copper brazed joints where a copper-tin-nickel-phosphorous (Cu-Sn-Ni-P) alloy was used as the filler metal. Post-examination by cross-sectioning the brazed joint revealed that a higher number of joint defects (i.e. the number of voids) were found for the joint prepared with a P400 interface roughness, compared to the specimens prepared down to P1000. It was reported by Wang et al. [7] that the detrimental effect of the coarser interface roughness was attributed to the lack of effective wetting of the surface. This explanation was consistent with the numerical simulation of equilibrium liquid configuration on and between rough surfaces [8]. Furthermore, it was reported by Leinenbach et al. [9] that brazed joints are susceptible to the formation of planar defects. These defects act as stress raisers and can reduce the joint strength remarkably. It then became reasonable to postulate that the presence of defects could reduce the HCF lives of brazed joint significantly. Therefore, the influence of defect on fatigue property and the criticality of defect area on fatigue life reduction needs to be assessed to ensure safety.

This paper aims to provide a systematic study about the effect of joint interface roughness and defects on the HCF life of SS brazed joints where pure copper was used as the filler metal. The interface roughness conditions include P80, P180, P240, P400, P800, P1200 and colloidal silica polishing (OPS). We describe characterisations of microstructures of the brazed joint, static strength, as well as HCF properties under the presence of joint defects. The impact of joint defects on the reduction in the HCF life is interpreted semi-quantitatively based on the stress intensity factor (SIF) range that considers both the defect area and the cyclic stress amplitude.

2. Materials and experimental procedures

2.1 Surface preparation

Type 304 austenitic stainless steel was used as the base metal. Table 1 shows the nominal chemical composition provided by Rapid Metals Ltd, UK. The filler metal was 25 µm thick copper foil with 99.999% purity provided by Alfa Aesar, Thermo Fisher Scientific, UK. The SS was originally supplied in the form of 12 mm diameter round bars and was subsequently sliced in segments of approx. 40 mm long for brazing fabrication.

Table 1 Nominal chemical composition of Type 304 stainless steel

Base metal	Chemical composition (wt.%)							
Type 304 stainless steel	Ni	Cr	Mn	Si	C	P	S	Fe
	9.25	19.00	2.00	1.00	0.08	0.05	0.03	Balance

Prior to brazing, the bonding surfaces of the SS samples were prepared using SiC papers to obtain different interface roughness conditions: P80, P180, P240, P400, P800, P1200 and OPS. For the OPS surface preparation, the SS was firstly ground down to P1200, followed by mechanical polishing using 9 µm, 3 µm and 1 µm diamond suspensions and finally polished by OPS for approx. 5 mins. This helped to provide an ultra-fine surface finish (i.e. deformation-free surface), as stated elsewhere [10]. Sample batch ID 1 to 7 denotes each interface roughness condition, as presented in Table 2. For example, batch 3 indicates brazed joints for which the joint interface was prepared with P240. The surface roughness, R_a, is defined as the average roughness of both the microscopic peaks and valleys for a specific joint interface condition. Five points were considered for each interface condition. A white light interferometer was utilised for the measurement of each interface roughness.

Table 2 Summary of batch ID, interface roughness, brazing condition and fatigue test parameters

Batch ID	1	2	3	4	5	6	7	8
Interface roughness	P80	P180	P240	P400	P800	P1200	OPS	SS
Brazing condition	1120 °C for 10min, joint clearance of 25 µm							
Fatigue test conditions	σ_a=135 MPa and σ_a=180 MPa, R=0.1, 20 Hz							

After obtaining the pre-defined interface roughness, the base metal was degreased and cleaned with acetone in an ultrasonic bath for 10 mins. The schematic diagram in Fig. 1 shows the sample fabrication process where the 25 µm copper foil was cut into 12 × 12 mm^2 disc and then placed between two pieces of stainless steel coupons with 40 mm long for each, Fig. 1(a). The assembly was then mechanically clamped together, as shown in Fig. 1(b). The periphery of each joint assembly was also tack welded to hold the pieces together during brazing; the two dots in Fig. 1(b) indicate the location of the tack welds.

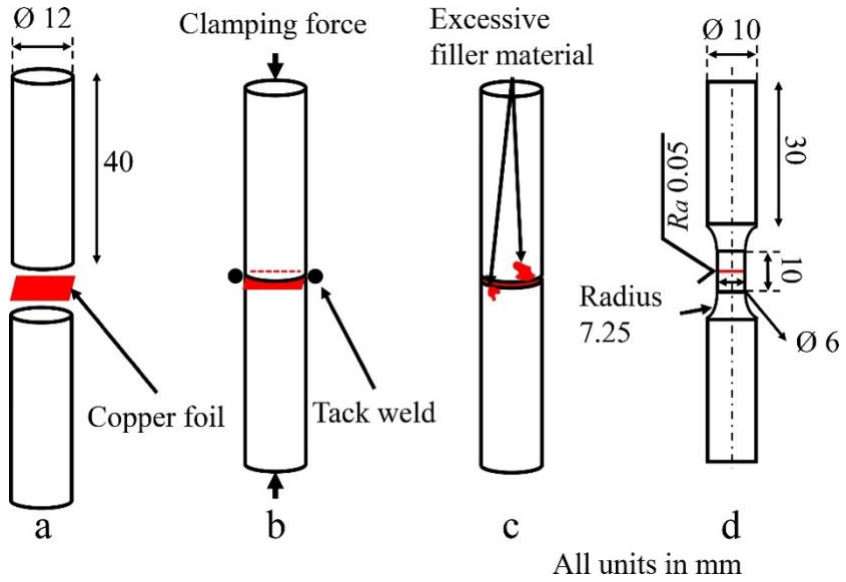

Figure 1: A schematic diagram showing the brazed joint fabrication process and mechanical test specimen extraction; (a) set up of copper filler metal; (b) tack welding process; (c) as-brazed condition; (d) final machined specimens for mechanical testing under static tension and fatigue loads

2.2 Brazing process

Brazing was performed in a conveyor belt furnace at the temperature of 1120 °C under hydrogen atmosphere. Fig. 2 shows the thermal history of a typical brazing process, which included three primary stages: heating, brazing and cooling. The initial temperature increase in Fig. 2 was related to the flame curtain that occurred when the tack welded sample assembly as shown in Fig. 1(b), moved close to the entrance of the heating zone of the brazing furnace. The flame curtain was used to ensure a reduced atmosphere. During the heating stage, the temperature rapidly increased from ~200 to 1080 °C within 6 mins. The sample assembly was then kept at the brazing temperature of 1120 °C for 10 mins. This ensured that a good wetting of the molten filler metal can be achieved. After the brazing stage, the sample assembly was cooled to room temperature within 30 mins, as presented in Fig. 2. This brazing process applied to all the specimens summarised in Table 2. After the entire brazing process, excessive copper filler metals might be produced from the edge of the designed brazed joint, as illustrated schematically in Fig. 1(c). To eliminate the interference of the excessive filler metal as well as the tack welds on the subsequent mechanical testing, the as-brazed

joint sample was then machined to the final dimension required for both the tensile and HCF testing. The testing specimen had a parallel gauge length of 10 mm and a diameter of 6 mm within the gauge section, as shown in Fig. 1(d).

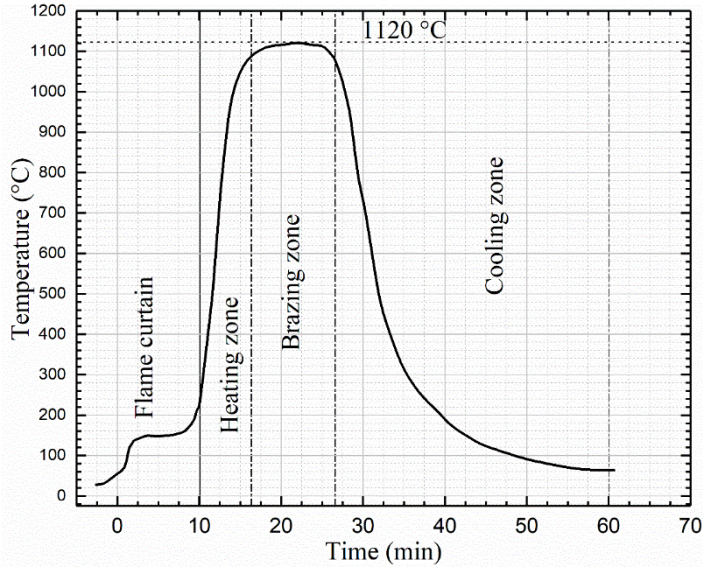

Figure 2: Thermal history of the entire brazing process

2.3 Joint microstructure examination

To examine the brazed joint microstructure, the sample assembly was sectioned along the axial direction as indicated by the dash line in Fig. 1(d). The sample cross-sections were then subjected to metallographic preparations, that included grinding up to P2500, polishing up to 1 µm diamond solution, and finally OPS polishing using a vibro-polisher for 12 hours with 0.02 µm colloidal silica. The prepared sample cross-sections were then examined by a scanning electron microscope (SEM, Zeiss Gemini) equipped with an energy dispersive X-ray spectrometer (EDS). Joint microstructure was revealed using back-scattered electron detector (BSE) under an accelerating voltage of 5 kV. EDS analysis with 20 kV was adopted to obtain the chemical composition of the brazed joint in both the point analysis and area mapping modes. Five individual point analysis measurements were performed, and the average value is reported. At least one sample assembly per batch (1-7) was prepared and then subjected to microstructural characterisation.

2.4 Tensile and fatigue testing

Tensile tests were conducted on brazed joint batches 1-7 each with different interface roughness conditions ranging from P80 to OPS, Table 2, to evaluate the effect of joint interface roughness on ultimate tensile strength (UTS). The determined UTS values would also help to select appropriate stress amplitudes for HCF tests. Tensile tests were performed on an Instron 8802 servo-hydraulic testing system with a 100 kN load cell. Tests were conducted at room temperature under a constant crosshead speed of 0.5 mm/min. At least two specimens were tested for each interface roughness condition and the average value is reported.

HCF tests were conducted using a constant stress amplitude sinusoidal waveform on the same testing system as mentioned above. The cyclic stress ratio was set to R=0.1 and the frequency was 20 Hz. Two stress amplitudes were selected, σ_a=135 MPa and σ_a=180 MPa as indicated in Table 2, to assess the HCF lives of the brazed joints. The maximum fatigue stress level was selected as 60% and 80% of the average UTS values of tensile test specimens. This led to the fatigue life being in the range of 10^4 to 10^6 cycles. The transition from low cycle fatigue to high cycle fatigue occurs at a fatigue life greater than ~10^4 cycles.

Five joint specimens were fatigue tested for each interface roughness condition ranging from P80 to OPS at both stress amplitudes (batch 1 to 7, Table 2). To enable a direct comparison of the fatigue properties between the brazed joint and base metal, three additional specimens of Type 304 stainless steel (batch 8, Table 2) were also fatigue tested at σ_a=180 MPa. The base metal specimens were subjected to the same heating and cooling cycle as applied to the brazed joint specimen. To mitigate the effect of machining [11], surfaces within the gauge section of each fatigue test specimen were ground by SiC paper up to P2500 prior to performing HCF fatigue tests, providing a R_a value of 0.05 μm, as indicated in Fig. 1(d).

2.5 Post-test examination

After fatigue tests, the fracture surfaces (batch 1-7) were examined by using SEM. A particular focus was to distinguish the fatigue crack initiation, propagation and final fracture zone, as well as to identify the presence of joint defects. In addition, high-resolution SEM images were collected, and ImageJ software was then used to provide

a quantitative measure of the joint defect areas within the fatigue crack initiation region. Due to the complex shape of the observed joint defect, a smooth perimeter was outlined around the defect region and the area of that shape was measured to provide an equivalent defect area. For defect-bearing specimens, fatigue striation spacings in the early-stage of fatigue crack propagation, i.e., close to the crack initiation region, were measured to provide an indicative evaluation of the initial fatigue crack growth rate. At least twenty measurements were made per sample condition to determine the average value of the fatigue striation spacings. EDS analysis was also performed on the fracture surfaces within the fatigue crack initiation zone. It was performed in the same way as for the joint microstructural characterisation. In addition, longitudinal cross-sections of the fractured specimens were examined using SEM to assist in understanding the fatigue failure mode of the brazed joint.

3. Results

3.1 Interface roughness and tensile strength of brazed joints

Fig. 3(a) presents the surface roughness R_a values as a function of different surface preparation conditions. As can be seen in Fig. 3(a), surface roughness values decreased rapidly from P80 (R_a=0.963 μm) to P400 (R_a=0.189 μm), whereas there was little difference in R_a values between P400, P800 and P1200. The surface polished down to OPS showed the minimum R_a value of about 0.005 μm, Fig. 3(a). In addition, it is evident that a coarser surface preparation led to a relatively large standard deviation (STDEV), whereas a finer surface preparation led to a much smaller STDEV, Fig. 3(a). The insets in Fig. 3(a) illustrate the coarsest (P80) and finest (OPS) interface roughness conditions revealed by SEM. Grinding marks were readily visible on the sample surface prepared by P80. On the other hand, the surface prepared down to OPS level showed no traceable marks and grain structures can be seen without the need of additional etching process.

The UTS values of brazed joints from batch 1 (P80) to 7 (OPS) are given in Fig. 3(b). The average tensile strength of the brazed joints that have been prepared from P80 to OPS are 508.5±26.2, 507.0±7.1 (P180), 508.5±14.8 (P240), 518.5±40.3 (P400), 520.0±14.1 (P800), 515.0±4.2 (P1200) and 503.5±12.0 MPa, respectively. No significant difference in UTS values can be seen for the brazed joint prepared with

different interface roughness conditions. This indicates that joint interface roughness of the base metal did not affect the consequent tensile strength of the brazed joints. It was also found that all the brazed specimens failed entirely within the joint region.

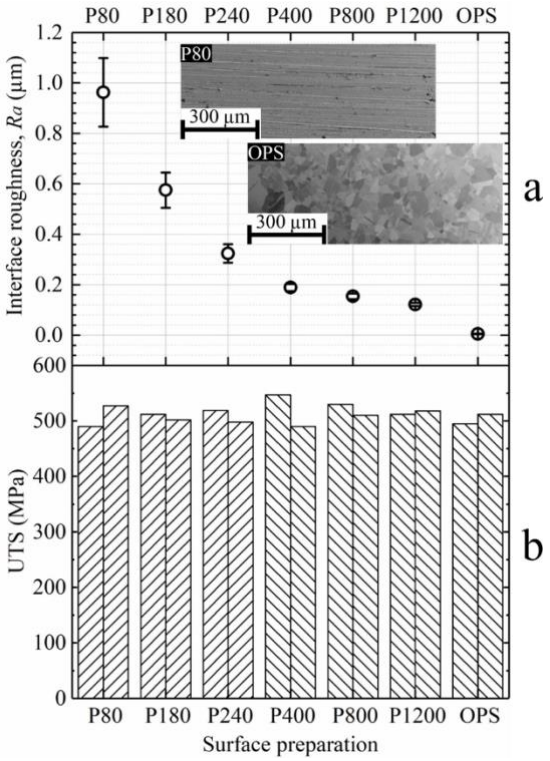

Figure 3: (a) Interface roughness (R_a) of the Type 304 stainless steel base metal prepared using various P-grade SiC papers and OPS polishing; (b) the ultimate tensile strength (UTS) of brazed joints with joint interface prepared to different roughness conditions

3.2 Joint microstructure and elements distribution

Microstructures of the brazed joints with different interface roughness were examined together with the measurement of the joint thickness. Fig. 4 displays the cross-sectional view of a brazed joint, batch 3 (P240). It can be observed that the brazed joint is relatively uniform with a typical thickness of around 25 μm; this agrees very well with the designed joint clearance, Fig. 1(b). The copper grain size within the joint region was measured to be 62.3±0.5 μm using the intercept method. Joint microstructures for those that had been prepared to various interface roughness values were found to be identical, hence only batch 3 sample is shown here as an exemplar.

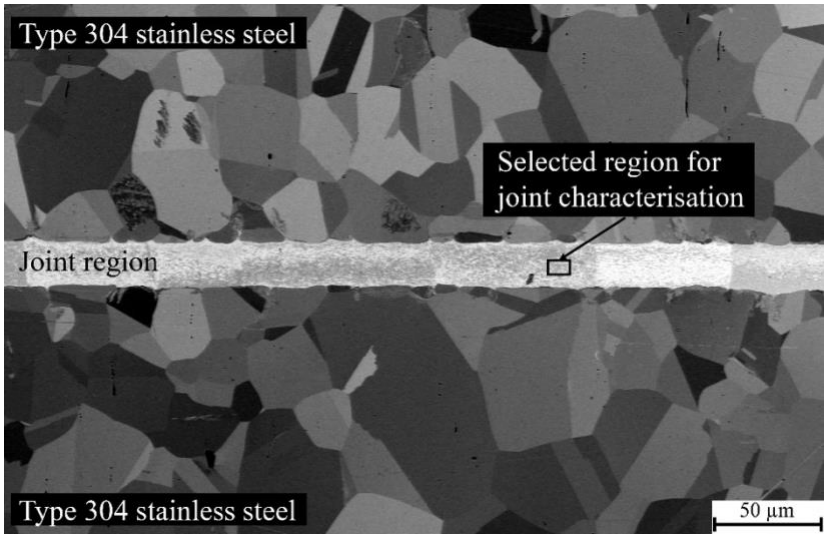

Figure 4: Microstructure of Type 304 stainless steel brazed joints using pure copper as the filler metal

Fig. 5(a) shows the microstructural features of the boxed region in Fig. 4 at a higher magnification. Two primary phases were found within this region, the copper matrix and star-shaped particles. Fig. 5(b) to 5(f) show the corresponding EDS elemental mapping of the selected region in Fig. 5(a). It is apparent that manganese and nickel elements, Fig. 5(e) and 5(f), were evenly distributed through the joint region, whereas the amount of chromium and iron, Fig. 5(b) and Fig. (c), were location dependent, with significant concentrations at the star-shaped regions. Thus, star-shaped particles were rich in chromium and iron while relatively lean in copper when compared to the copper matrix, Fig. 5(d). The average elemental contents of the selected EDS region in Fig. 5(a) is given in Table 3; it contained ~93.9% Cu, 3.7% Fe, 0.7% Cr, 1.2% Ni and 0.5% Mn (all in wt.%). In addition, EDS point analyses were performed at two typical locations; points 1-4 for the copper matrix and points 5-8 for the star-shaped particles, Table 3. The copper matrix in Fig. 5(a) contained ~96.1 wt.% Cu, 1.9 wt.% Fe, 0.3 wt.% Cr, 1.2 wt.% Ni and 0.5 wt.% Mn, while the star-shaped particles contained ~77.3% Cu,16.5% Fe, 3.8% Cr, 1.8% Ni and 0.6% Mn (all in wt.%). These point analysis results were consistent with the area mapping in terms of showing that the star-shaped particles were rich in both iron and chromium elements. The average size of the star-shaped particles was determined to be 0.43±0.03 µm. Steward et al. [12] conducted brazing of Type 304 stainless steel to vanadium alloys using copper. Iron-copper-rich precipitates with similar morphology were found in their work. Therefore, the particles obtained in the current work are very likely to be intermetallic Cr-Fe-Cu precipitates.

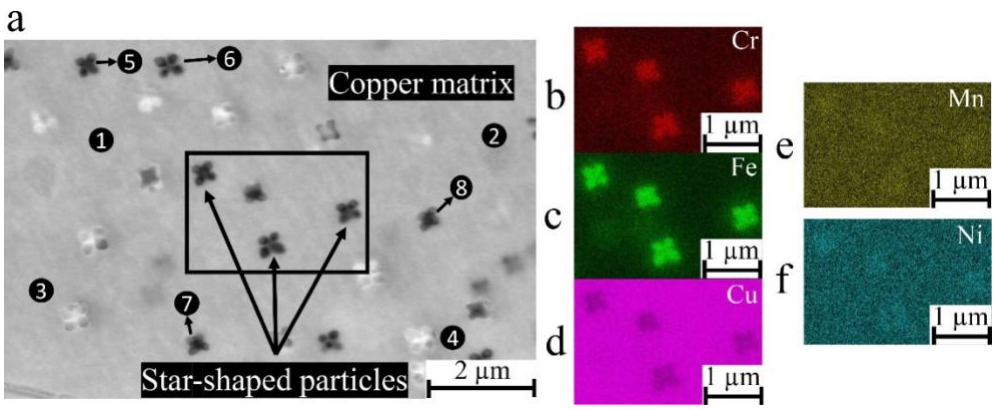

Figure 5: (a) Microstructure of Type 304 stainless steel brazed joints; EDS elemental mapping of (b) chromium Cr; (c) iron Fe; (d) copper Cu; (e) manganese Mn (e) and (f) nickel Ni of the selected rectangular region in (a)

Table 3 EDS data obtained by point analysis and area mapping at the boxed regions in Fig. 5(a) and Fig. 10(a). Points 1-4 and 5-8 represent the copper matrix and star-shaped particles within Fig. 5(a), respectively

EDS point analysis and area mapping	Composition (wt.%)				
	Cu	Fe	Cr	Ni	Mn
Point 1-4 (copper matrix)	96.10±0.44	1.93±0.47	0.33±0.15	1.17±0.06	0.50±0.10
Point 5-8 (particles)	77.25±0.52	16.50±0.56	3.80±0.14	1.83±0.05	0.63±0.05
EDS map in Fig. 5(a)	93.90	3.70	0.70	1.20	0.50
EDS map in Fig. 10(a)	94.90	2.70	0.90	1.00	0.50

Fig. 6(a) shows two copper-rich grains separated by a grain boundary within the brazed joint region. The grain on the left contained star-shaped (four petals) particles, while the one on the right contained three-petal-shaped particles. In addition, most particles within each individual grain possessed preferred orientations. This indicates that the shapes and orientations of the particles might be dependent on the grain orientation of the copper matrix, i.e., a possible fixed orientation relationship between the particles and copper grains, as illustrated by a schematic diagram in Fig. 6(b).

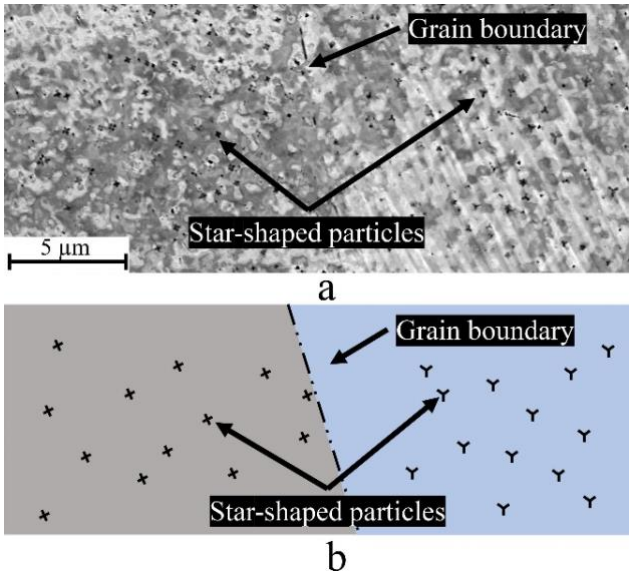

Figure 6: (a) Star-shaped particles formed at copper grains with different orientations; (b) a schematic diagram showing different shapes of the particles and a fixed orientation relationship between the particles and copper matrix

3.3 HCF properties and effect of joint interface roughness

The average HCF life of brazed joints with different joint interface roughness was assessed by considering five individual specimens per interface roughness condition. The HCF fatigue test results at the higher stress amplitude (σ_a=180 MPa) are shown in Fig. 7(a) to reveal the influence of interface roughness as well as the presence of defects. The brazed joints can be categorised into two groups, defect-free and defect-bearing, according to the post-test fracture surface SEM observation. It is evident from Fig. 7(a) that the joint interface roughness had negligible influence on the fatigue life of defect-free joints. The average fatigue life of the defect-free brazed joints was about 8×10^4 cycles. However, the defect-bearing specimens had lower fatigue life when compared to the defect-free ones, ranging from 1×10^4 to 5×10^4, Fig. 7(a). Furthermore, the defect-bearing brazed joints tended to have a large scatter in terms of the measured fatigue life; this particularly applied to interface roughness of P240 and OPS.

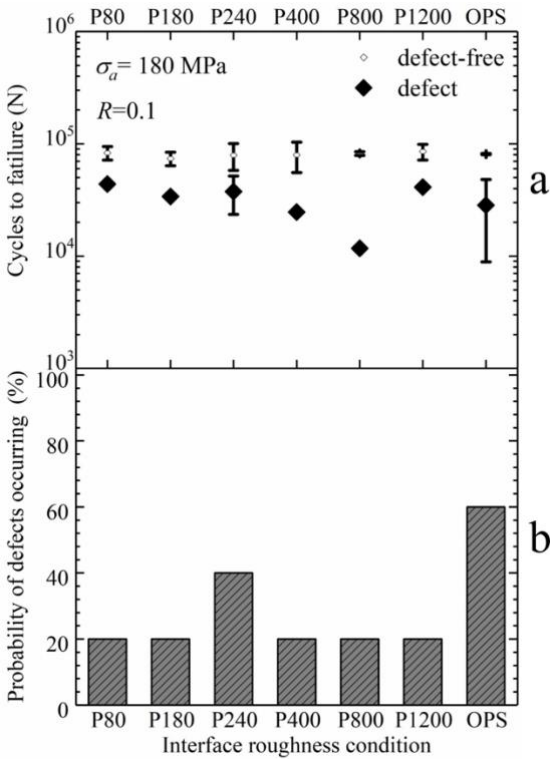

Figure 7: (a) Fatigue life of defect-free and defect-bearing brazed joints with different joint interface roughness conditions ranging from P80 to OPS; (b) the probability of defects occurring as a function of different interface roughness conditions

Fig. 7(b) shows the probability of defects occurring in specimens with various interface roughness conditions. The probability was calculated according to the proportion of the defect-bearing specimens within the total specimens per interface roughness condition. As shown in Fig. 7(b), the defect probability was 20% for P80, P180, P400, P800, and P1200 prepared joints. The brazed joints that had been prepared by P240 and OPS exhibited higher defect probability of 40% and 60%, respectively. However, the higher defect probability value of 40% for the P240 prepared brazed joints does not necessarily indicate poor wetting behaviour. This is because lower defect probability values were observed for both coarser (P80 and P180) and finer (P400-P1200) interface conditions. For brazed joints prepared by OPS, the probability of defect occurring was significantly higher than the other interface conditions. This observation could be attributed to limited wetting, which was reported in wetting behaviours of AgCu/Cu systems [13]. In summary, interface roughness of OPS led to an increased likelihood to generate joint defects during brazing, hence being responsible for the relatively large scatter in the fatigue life, Fig.7(a).

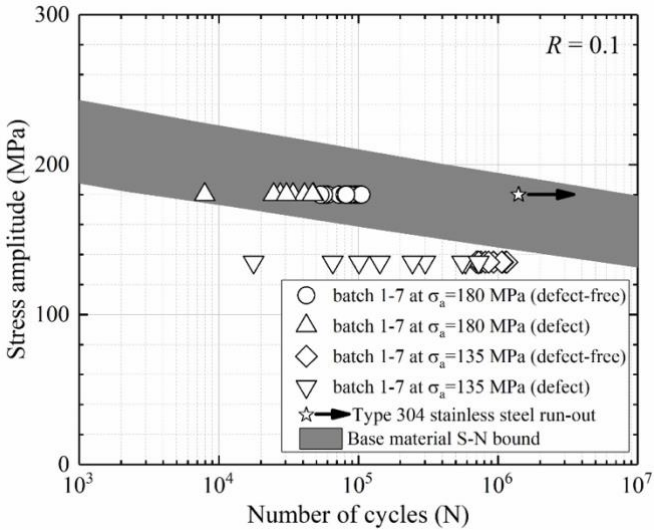

Figure 8: Summery of HCF life for batch 1-7 specimens tested at two different stress amplitudes, compared with the base metal (batch 8) fatigue life and S-N data band for Type 304 stainless steel [14]

Fig. 8 presents the HCF fatigue life of sample batch 1 to 7 at two stress amplitudes (σ_a=135 MPa & σ_a=180 MPa), for both the defect-free and defect-bearing specimens. As shown in Fig. 8, the maximum fatigue life of brazed joints subjected to σ_a=135 MPa approached 10_6 cycles, whereas the fatigue tests conducted at σ_a=180 MPa failed within 10_5 cycles. In addition, defect-bearing specimens always had a lower fatigue life when compared to the defect-free counterparts. This applied to both the higher stress amplitude of σ_a=180 MPa and the lower stress amplitude of σ_a=135 MPa fatigue tests, Fig. 8. Furthermore, the defect-free specimens exhibited less data scatter in the HCF fatigue life when compared to the defect-bearing ones. The grey band in Fig. 8 is the S-N data bounds of Type 304 stainless steels providing a comparison to the brazed joint specimens. Three base metal fatigue specimens made from the same Type 304 stainless steels were tested at the stress amplitude of σ_a=180 MPa; all the three base metal specimens did not fail after $3 \times 10_6$ fatigue cycles, thus fatigue run-out was indicated in Fig. 8. This suggests that brazed joints tended to have a lower HCF life when compared to the base metal.

3.4 Fractography

After the completion of fatigue tests, it was observed by naked eyes that all the brazed specimens failed within the joint region. Since the presence of joint defects was found to dominate the fatigue life of the brazed joints, SEM fractography examination was performed to further understand the joint failure mechanism. Fig. 9 shows two typical types of fracture surfaces that were observed for all the brazed joint specimens; fatigue cracks initiated either from the specimen surface, see Fig. 9(a), or from the joint defect, see Fig. 9(b). SEM images of both fatigue crack initiation regions at higher magnifications are given in Fig. 9 (c) and 9 (d), respectively. For the defect-free brazed joint specimens, fatigue cracks were exclusively found to initiate from the specimen surface.

Also shown in Fig. 9 (a) and 9 (b) are the fatigue crack propagation and final fracture zones. There was no difference between the defect-free and defect-bearing specimens in terms of the fatigue crack propagation and final fracture zones, whereas the defect-bearing specimens had a relatively large fatigue crack initiation region when compared to that of the defect-free ones. A large number of dimples were present at the final fracture zones for both the defect-free in Fig. 9(a) and defect-bearing specimens in Fig. 9(b). The presence of dimples suggests that these fatigue specimens finally failed by a typical ductile mode that involved void nucleation, growth, and coalescence, because the remaining areas could no longer sustain the maximum stress applied.

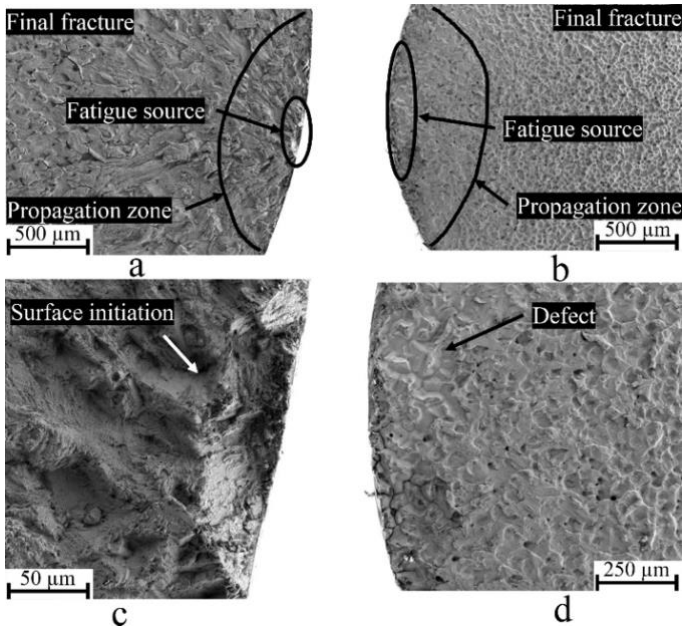

Figure 9: Fracture surfaces of (a) defect-free and (b) defect-bearing joints; (c) enlarged view of (a) fatigue crack initiated from the sample surface; (d) enlarged view of (b) fatigue crack initiated from the joint defect. Both samples are from batch 7 (OPS)

Fig. 10 shows the defect region within the fatigue crack initiation zone of the same sample (batch 7) at a higher magnification, together with the EDS area mapping. The relatively smooth regions in Fig. 10(a) were considered as the joint defect, likely to be an incomplete fusion type [15]. Texture patterns with different sizes can also be seen within these defect regions, Fig. 10(a). Fig. 10(b) to 10(d) show the corresponding EDS elemental mapping of the selected rectangular box in Fig. 10(a). It is apparent that the distribution of chromium and iron, Fig. 10(b) and Fig. 10(c), were location dependent and associated with the texture patterns. Copper was found to be rich in the whole region but relatively lean in the texture patterns, Fig. 10(d). The average element distribution of the selected EDS region in Fig. 10(a) is given in Table 3; the texture patterned region contained ~94.9% Cu, 2.7% Fe, 0.9% Cr, 1.0% Ni and 0.5% Mn (all in wt.%). These chemical compositions revealed in Fig. 10(a) were very close to those observed in the selected region in Fig. 5(a), indicating that the star-shaped particles observed in Fig .5(a) might be the imprints of these texture patterns.

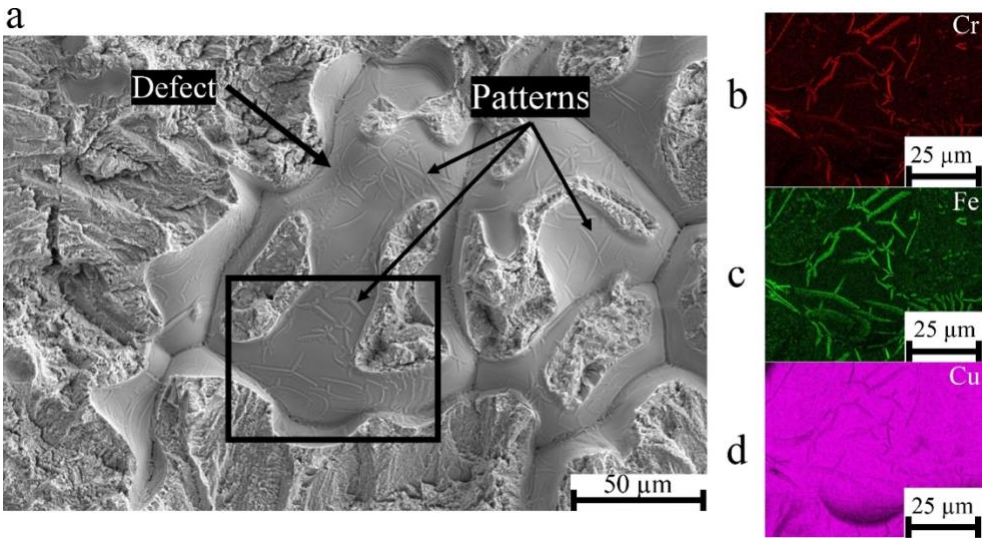

Figure 10: (a) Defect region and texture patterns within the fatigue crack initiation zone (batch 7); EDS elemental mapping of (b) chromium Cr; (c) iron Fe and (d) copper Cu of the selected rectangular region in (a)

Fig. 11 shows the typical fatigue striations for the defect-bearing specimens with various defect areas. Five specimens with distinctive initial fatigue striation spacings were selected and illustrated in an ascending order in Fig. 11. Fig. 11(a) shows the minimum fatigue striation spacing, whereas the maximum fatigue striation spacing is shown in Fig. 11(e); intermediate fatigue striation spacings are presented in Fig. 11(b) to Fig. 11(d). The fatigue striations within the early-stage of fatigue crack propagation, i.e. close to the fatigue crack initiation region, were measured to provide an indication of the initial fatigue crack growth rate. The specimens with the smallest defect area of A=0.03 mm^2 (batch 7A) had a corresponding initial fatigue striation spacing of 0.09±0.02 µm, Fig. 11(a). Similarly, the initial fatigue striation spacing for the specimen with the largest defect area A=1.47 mm^2 (batch 6B) was measured to be 0.54±0.05 µm, Fig. 11(e). The fatigue striation spacing values and the corresponding defect areas are summarised in Table 4. It is evident that the initial fatigue striation spacings were positively dependent on the magnitude of the defect areas. For the defect-bearing brazed joints, a larger joint defect led to a higher initial fatigue striation spacing, i.e., a higher initial fatigue crack growth rate.

Table 4 Typical joint defect areas and corresponding initial fatigue striation spacings measured from fractography of fatigue test samples (σ_a=180 MPa). Also shown in this table are the calculated stress intensity factor range as a function of defect area and applied stress ranges. Batch ID A & B represents two individual specimens that have the same interface roughness conditions

Batch ID	7A	6A	3A	7B	6B
Defect area A (mm^2)	0.03	0.05	0.17	0.60	1.47
Initial striation spacing (μm)	0.09±0.02	0.12±0.02	0.19±0.02	0.26±0.01	0.54±0.05
SIF range ΔK (MPa√m)	5.50	6.17	8.44	11.56	14.43

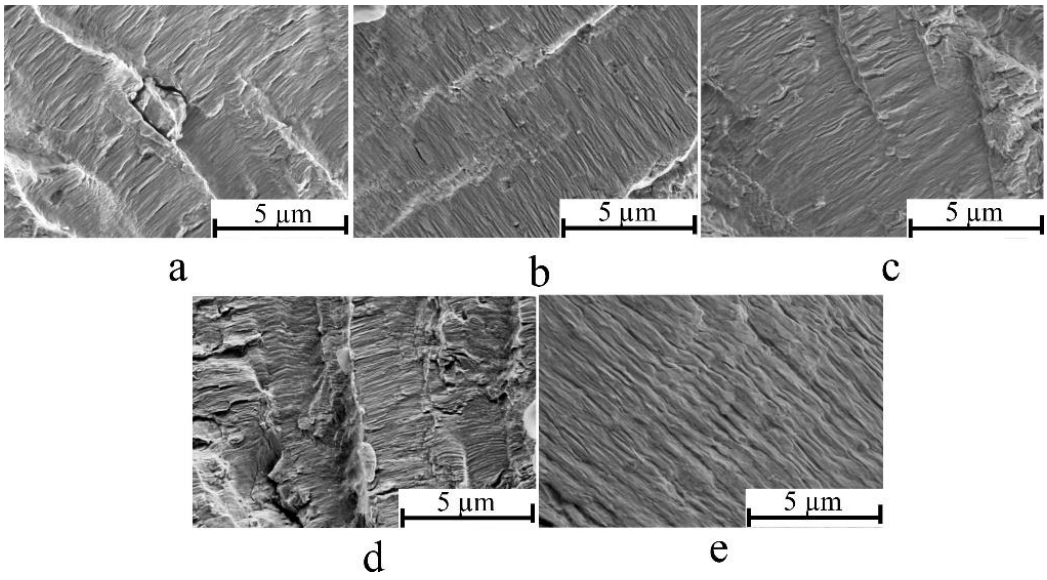

Figure 11: Fatigue striation spacings at the early-stage fatigue crack propagation regions of defect-bearing samples with an initial defect area of (a) A=0.03 mm^2, batch 7A; (b) A=0.05 mm^2, batch 6A; (c) A=0.17 mm^2, batch 3A; (d) A=0.60 mm^2, batch 7B; and (e) A=1.47 mm^2, batch 6B. Batch ID A & B represents two individual specimens that have the same interface roughness conditions

4. Discussion

4.1 Precipitation

Chen et al. [16] investigated the casting process of copper and copper alloys with small amount of impurity elements. Additional iron (≤1.5 wt.%) was added into copper and its alloys during casting to form iron-rich nanoparticles with an average size of 6 nm to create precipitation hardening effect. Chen et al. [17] also successfully identified two distinct morphologies of iron-rich nanoparticles in Cu-10Sn-2.0Zn-1.5Fe-0.5Co alloys: (i) near-spherical-shaped (face-centred-cubic, fcc crystal structure) nanoparticles with size ranges from 2 to 20 nm in diameter and (ii) star-shaped (fcc) nanoparticles with size ranges from 20 to 150 nm. However, larger sized star-shaped nanoparticles of between 250 and 500 nm with a body-centred-cubic (bcc) crystal structure were observed when extra iron was added, reported in [18].

According to Fig. 5(a) and the corresponding EDS area mapping, the average iron content measured within the joint microstructure was 3.70 wt.%, Table 3. In addition, the average size of the observed star-shaped particles was about 400 nm, Fig. 5(a). Three primary reasons could be responsible for the formation of large sized iron-rich nanoparticles in the present stainless steel brazed joints. Firstly, iron content strongly influences the morphology and size of the nanoparticles; the nanoparticles coarsen with the increase of iron content; this seems to be consistent with the previous findings in [18] where star-shaped particles were found for Cu-2.0Fe-0.5Co and Cu-3.0Fe-0.5Co alloys with sizes of ~200 nm and ~300 nm, respectively. It was also claimed by Chen et al. [18] that iron-rich nanoparticles would undergo a spherical-to-star shape transition when iron content was higher than 2.0 wt%. Secondly, alloying elements affect the formation of star-shaped nanoparticles; it was found that all the iron-rich nanoparticles were near-spherical-shaped for Cu-1.5Fe-0.5Co alloy, whereas the star-shaped nanoparticles sized from 20 to 150 nm were observed in Cu-10Sn-2.0Zn-1.5Fe-0.5Co alloy. In our case, chromium element was found to be associated with the star-shaped particles. Hence, it is likely to conclude that chromium tends to promote the formation of star-shaped particles in stainless steel brazed joints where copper is used as filler metal. Thirdly, the brazing cycle (Fig. 2) utilised a relatively slow cooling rate of about 130 °C/min, when compared to the cooling rate of 100 °C/s for the copper alloy casting

process. The prolonged cooling cycle in brazing could potentially serve as an aging process that led to the coarsening of iron-rich nanoparticles [17].

In brief, the precipitation evolution observed in the present brazed joint can be summarised as follow. At the brazing temperature of 1120 °C, approx. 3.70 wt.% iron migrated from the base metal (SS) into liquid copper through high-temperature diffusion within the brazing period, Fig. 2. At the beginning of cooling, iron started to precipitate out from the liquid copper as spherical nanoparticles with fcc crystal structure. During the continuous and slow cooling, the fcc iron-rich precipitates grew and finally transformed into star-shaped precipitates with a bcc crystal structure.

As shown in Fig. 5(a), the copper filler metal was no longer chemically homogeneous after the brazing process. Foreign elements, such as iron, nickel, manganese and chromium all diffused from the base metal into the joint region as a result of high-temperature diffusion. Both the chromium and iron contents were found to be location dependent; being rich in those star-shaped particles shown in Fig. 5(b) and Fig. 5(c). A similar observation of the particles has been reported in [19] where fine iron-rich particles were found in copper with the same morphology. Steward et al. [12] also suggested that these particles were iron-rich precipitates mostly being $FeCu_2$ and $FeCu_{18}$, determined by wavelength-dispersive X-ray spectroscopy. According to the EDS point analysis performed on the star-shaped particles, Fig. 5(a) and Table 3, the iron-rich particles had a similar chemical composition close to that of formula $FeCu_4$ (ICDD-PDF 03-065-7002) [20]. Similar nanoparticles with an average size of 350 nm were also reported as $FeCu_4$ phase by Shu et al. [21] when performing gradient deposition of copper on stainless steels.

It is worthwhile to note that only iron-rich nanoparticles have been reported to precipitate in copper matrix according to the work performed by Klein et al. [22]. Conversely, a measurable amount of chromium (3.8 wt.%) was also detected at the iron-rich nanoparticles but not at the copper matrix, Table 3. According to the Fe-Cu, Cr-Cu binary phase diagrams, copper can dissolve up to 3.5 wt.% iron and 2.0 wt.% chromium at the brazing temperature of 1120 °C. The joint region contained on average ~3.7 wt.% iron and ~0.7 wt.% chromium according to the EDS area mapping, Table 3. The amount of iron (3.7 wt.%) that diffused from the base metal into the joint region agrees well with that in the Fe-Cu phase diagram (3.5 wt.%). However, the amount of chromium (0.7 wt.%) within the joint region was only less than half of the equilibrium value (2.0 wt.%). This could be attributed to the differences in concentrations of iron (~70 wt.%)

and chromium (~19 wt.%) in the base metal, Table 1. In other words, there was less chromium within the base metal to diffuse into the copper filler metal. Nevertheless, both iron and chromium are almost immiscible in copper at room temperature and Chbihi et al. [23] has reported that chromium could precipitate out from copper matrix of Cu–1Cr–0.1Zr (wt.%) with a fcc crystal structure. Therefore, the observed star-shaped particles within Fig. 5(a) are precipitates being rich in copper, iron and chromium.

4.2 Precipitation hardening

For both tensile and HCF tests, all the specimens failed entirely within the brazed joint region in the present study. Therefore, the tensile strength obtained reflects the mechanical behaviours of the joint region. The UTS of the stainless steel brazed joints was found to be around 500 MPa, Fig. 3. This value is well beyond the UTS of pure copper, which varies from 200 to 250 MPa [24]. Strengthening mechanism of copper and its alloys can be categorised into three primary types, nanocrystalline copper, bimodal structure copper and so-called nanostructured copper. The nanostructured copper refers to copper and copper alloys with micrometre-sized grains (20 to 60 μm) embedded with nanoparticles with a typical size of 2 to 10 nm [16]. Among the three types of strengthened coppers, only nanocrystalline copper [25] and nanostructured copper [26] could provide UTS values well above 500 MPa. However, microstructure examination in the present study revealed an average copper grain size of 62.3±0.5 μm within the brazed joint region, Fig. 4. Therefore, the only possible strengthening mechanism that could explain the high magnitude of tensile strength (UTS) is the so-called nanostructured copper. For example, Chen et al. [16] has stated that homogeneously distributed iron-rich nanoparticles of 2 to 10 nm with fcc crystal structure is able to strengthen copper/copper alloys. This was caused by the high density of geometrical dislocations as a consequence of the coherent interface between the nanoparticles and the copper matrix. However, a larger precipitate size and possibly smaller precipitate number density was observed in the present study, which might result in a loss of coherency and therefore compromise the precipitation hardening effect, as stated elsewhere [18]. It is therefore postulated that a reduced precipitation hardening effect is mainly responsible for the obtained UTS of the brazed joints.

4.3 Failure mode

Suezawa [27] has concluded that the strength of brazed joints can be altered by introducing various joint interface roughness conditions. This is because different interface roughness conditions would essentially provide distinct bonding areas, i.e. relatively rough joint interfaces should lead to stronger brazed joints. Fig. 12 shows the longitudinal view of fractured specimens (batch 1, 2 and 7, Table 2) after HCF tests. Residual filler metals were exclusively found on the fracture surfaces of all the three fatigue specimens that had been prepared to P80, P180 and OPS interface roughness conditions, respectively. However, no visible separations or cracks could be revealed at the copper/stainless steel interface, Fig 12. This indicates that both the fatigue crack initiation and propagation occurred entirely within the filler metal region. The prepared joint interface roughness might have altered the strength of the copper/stainless steel interface, but surely did not affect the filler metal itself. Therefore, brazed joint interface roughness conditions had little effect on the joint fatigue life.

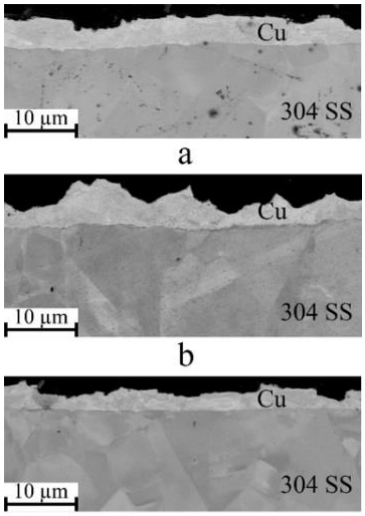

Figure 12: Longitudinal sections of the fatigue fractured samples, (a) from batch 1 (P80), (b) from batch 2 (P180) and (c) from batch 7 (OPS)

4.4 Influence of defects on joint fatigue performance

According to Fig. 9(b), fatigue cracks always initiated from the defect regions for the defect-bearing brazed joints. Defects within the brazed joints occupied a small fraction of the overall joint. For example, Fig. 13 shows the fracture surface of a

specimen from batch 2 (P180 prepared). The area fraction of the final fracture zone was about 85% of the overall designated joint region, whereas the defect fraction was only about 0.2%. If we treat the defect as a pre-existing crack, the crack could grow gradually under the fatigue loading cycles leading to the final fracture.

The insets within Fig. 13 represent two fatigue specimens where cracks initiated from defects of different sizes. If we assume the area fractions of the final fracture zones are the same for both cases, then the number of cycles needed for the fatigue crack propagation should be different, i.e. the propagation distances for both cases should be different. The fatigue crack propagation distance for the specimen with a larger initial defect would be shorter than that for the specimen with a smaller defect. This fatigue crack propagation distance is indicated in Fig. 13. Now the only unknown variable is the fatigue crack growth rate. The classic Paris law [28], Eq. (1) is therefore applied here to assist in understanding the initial fatigue crack growth rate in a qualitative way,

$$\frac{da}{dN} = C\left(\Delta K\right)^m \tag{1}$$

where the coefficient C and exponent m are the material constants, da/dN is the fatigue crack growth rate. It is clear that the initial fatigue crack growth rate for the defect-bearing joints is dependent on the stress intensity factor (SIF) range ΔK, which can be calculated according to the Murakami equation [29],

$$\Delta K = C_2 \times \Delta\sigma \times \sqrt{\pi \times \sqrt{A}} \tag{2}$$

where A is the projected defect area on a plane perpendicular to the maximum principal stress, and $\Delta\sigma$ is the applied cyclic stress range. According to literature, C_2 is 0.65 for surface defects [29]. The defects observed within this study were either surface or sub-surface defects, therefore C_2 of 0.65 is considered here. Hence, at the initial stage of the fatigue crack propagation, the fatigue crack growth rate can be expressed:

$$\frac{da}{dN} = C \times \left(C_2 \times \Delta\sigma \times \sqrt{\pi \times \sqrt{A}}\right)^m \tag{3}$$

where C, C_2, m, $\Delta\sigma$ and π are all constants, thus the initial fatigue crack growth rate can be simplified as a function of the initial defect area A. According to literature, in the linear elastic fracture mechanics (LEFM) regime, the exponent m is in the range of 3 to 5 for steels [30] and 2 to 4 for pure copper [31]. However, the initial crack size (Fig. 13) of about 0.2 mm should be considered as a short crack. Consequently, use of the Paris law is inappropriate. Nevertheless, it is convenient to plot short crack growth rate against ΔK as the presentation of the long crack data. Measured exponent m in Eq. (3) is greater for short cracks than long cracks under the same ΔK. From literature, m is higher for short crack but in the same magnitude as long cracks [32–34]. Therefore, it is reasonable using the Paris law for a qualitative interpretation. As a consequence, a higher initial fatigue crack growth rate would be expected for a specimen with a larger defect. Since the fatigue propagation distance is considerably short, a specimen with a larger defect would have a shorter fatigue life.

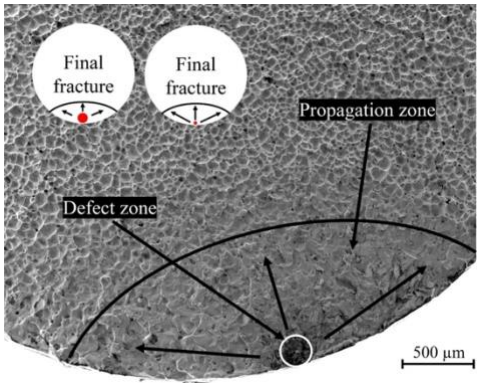

Figure 13: Fracture surface of a specimen from batch 2 (P180) showing the defect, fatigue crack propagation and final fracture zones; the insets illustrate fatigue samples where cracks initiated from either a large or a small defect.

The influences of brazed joint defects on the corresponding fatigue life are now considered semi-quantitatively. The actual relationship between the initial joint defect area and the corresponding fatigue life for all the HCF tested specimens at σ_a=180 MPa is shown in Fig. 14. The triangular symbols represent the defect-bearing brazed joints, whereas the circular symbols represent defect-free ones. It can be seen that the defect-bearing joints had much shorter fatigue life when compared to the defect-free ones. Also, the fatigue life of the defect-bearing joints dropped rapidly with the increase of defect areas. For example, the maximum defect area was measured to be ~1.47 mm^2,

whereas the corresponding fatigue life was below 10^3 cycles, Fig. 14. When the defect area decreased, the fatigue life increased and approached that of the defect-free ones. For instance, the defect-bearing specimens had fatigue life of ~4.8×10^4 cycles when the defects were sufficiently small, typically below 0.1 mm^2 in terms of the projection area. This value was relatively close to the lower limit of fatigue life of the defect-free specimens of ~5.2×10^4. The secondary vertical axis (Fig. 14) shows the calculated defect area fraction over the overall joint. This might be of a practical interest. For the defect-bearing specimens, the relationship between defect areas and corresponding fatigue life was also plotted on logarithmic scale as illustrated in the left inset in Fig. 14. Linear fitting was applied to reveal how the fatigue life decreased as the defect increased; the slope of the linear fitting was found to be around 1.52±0.25.

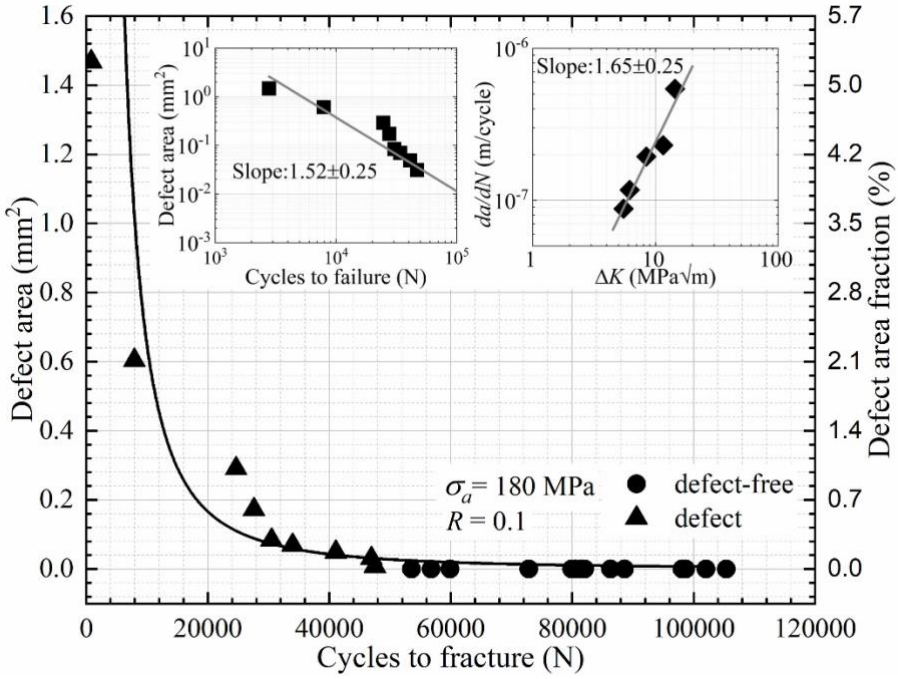

Figure 14: Relationship between the joint defect area and the corresponding fatigue life for all the fatigue tests performed at σ_a=180 MPa; the insets show the relationship between joint defect area and fatigue life, and the initial fatigue crack growth rate as a function of ΔK on logarithmic scales

Fatigue crack growth rate is defined as crack extension per load cycle, *da/dN*, as shown in Eq. 1. Fatigue striation spacings measured near the joint defect can therefore be considered as an indication of the initial fatigue crack growth rate, Fig 11. Hence, the initial fatigue striation spacing of a specimen with a larger defect should be much

greater than that with a smaller defect, owing to the larger defect area and hence larger stress intensity factor range ΔK. This was also revealed by the measurement of fatigue striation spacings on fracture surfaces of the defect-bearing specimens, Table 4. The corresponding ΔK values were also calculated and listed in Table 4 in an ascending order. In total, five ΔK values were considered here and it was found that ΔK increased from 5.50 MPa√m (batch 7A) to 14.43 MPa√m (batch 6B) when the corresponding initial defect area increased from 0.03 mm^2 to 1.47 mm^2, leading to an increase in the initial fatigue striation spacing from 0.09±0.02 μm to 0.54±0.05 μm, Table 4. The initial fatigue crack growth rate (da/dN) of the brazed specimens with various initial defect areas were also plotted against the corresponding SIF range (ΔK) on logarithmic scale, as shown in the right inset in Fig. 14. The slope of the linear fitting, providing the Paris law exponent m as shown in Eq. 3, was found to be 1.65±0.25, which agrees well with the lower bound of literature value of 2 to 4 for pure copper [31]. This suggests that a large joint defect, which leads to a higher SIF range ΔK, will result in a higher fatigue crack growth rate, hence shorten the fatigue life exponentially.

5. Conclusions

This work examined the microstructure of stainless steel joints processed by brazing. The influences of interface roughness and defects on joint properties were also critically investigated. Based on the results obtained the following conclusions can be made:

1. Star-shaped precipitates of ~ 400 nm was found in the brazed joint region. These particles were found being rich in iron and chromium but relatively lean in copper compared to the copper matrix. EDS measurement revealed a chemical composition of Cu-16.5Fe-3.8Cr-1.8Ni-0.6Mn for these precipitates. The copper to iron ratio suggests that they are very likely to be $FeCu_4$ phase.
2. The brazed joint showed higher tensile strength and HCF life when compared to pure copper. The mechanical enhancement was attributed to the precipitates within the joint region.
3. No significant difference in UTS values can be seen for the brazed joint prepared with different interface roughness conditions from P80 to OPS. This indicates that joint interface roughness did not affect the consequent tensile strength of the brazed joints on the ground that all the brazed specimens failed entirely within the joint region.

4. The joint interface roughness had negligible influence on the fatigue life of defect-free brazed joints. This was attributed to the fact that both the fatigue crack initiation and propagation happened entirely within the joint region.
5. For the defect-bearing brazed joints, larger defect led to a higher fatigue crack growth rate at the initial stage. Qualitatively, the fatigue cycles to failure was found to decrease with the increase of defect area (size).

Acknowledgement

BC acknowledges UK's Engineering and Physical Science Research Council, EPSRC, for financial support through the First Grant Scheme EP/P025978/1. YL acknowledges the assistance of Mr. Rizwan Tai, Mr. Steve Damms and Mr. Barry Meek, Coventry University, with the brazing specimens manufacturing.

This research did not receive any specific grant from funding agencies in the public, commercial, or not-for-profit sectors.

Data availability

The raw data required to reproduce these findings cannot be shared at this time due to technical or time limitations. The processed data required to reproduce these findings cannot be shared at this time due to technical or time limitations.

6. References

[1] M.A. Xavior, M. Adithan, Determining the influence of cutting fluids on tool wear and surface roughness during turning of AISI 304 austenitic stainless steel, J. Mater. Process. Technol. 209 (2009) 900–909.

[2] G.K. White, Thermal expansion of reference materials: copper, silica and silicon, J. Phys. D. Appl. Phys. 6 (1973) 2070.

[3] I. Kawakatsu, Y. Suezawa, Effects of surface preparations of base metal on the brazed joint strength, Trans. Japan Weld. Soeiet. 3 (1972).

[4] I.T. Hong, C.H. Koo, The study of vacuum-furnace brazing of C103 and Ti-6Al-4V using Ti-15Cu-15Ni foil, Mater. Chem. Phys. 94 (2005) 131–140.

[5] T. Zaharinie, Z. Huda, M.F. Izuan, M. Hamdi, Development of optimum process parameters and a study of the effects of surface roughness on brazing of copper, Appl. Surf. Sci. 331 (2015) 127–131.

[6] Y. Suezawa, Effects of surface roughness on the fatigue strength of brazed joint, Trans. Japan Weld. Soc. 7 (1976) 1677–1687.

[7] H. Wang, J. Cao, J. Feng, Brazing mechanism and infiltration strengthening of CC composites to TiAl alloys joint, Scr. Mater. 63 (2010) 859–862.

[8] C.C. Bartlow, Numerical simulation of equilibrium liquid configurations On and between rough surfaces. PhD thesis, University of California, 2011.

[9] C. Leinenbach, M. Koster, H.J. Schindler, Fatigue assessment of defect-free and defect-containing brazed steel joints, J. Mater. Eng. Perform. 21 (2012) 739–747.

[10] B. Chen, J.N. Hu, P.E.J. Flewitt, A.C.F. Cocks, R.A. Ainsworth, D.J. Smith, D.W. Dean, F. Scenini, Effect of thermal ageing on creep and oxidation behaviour of Type 316H stainless steel, Mater. High Temp. 32 (2015) 592–606.

[11] T. Poulain, J. Mendez, G. Hénaff, L. de Baglion, Analysis of the ground surface finish effect on the LCF life of a 304L austenitic stainless steel in air and in PWR environment, Eng. Fract. Mech. 185 (2017) 258–270.

[12] R.V. Steward, M.L. Grossbeck, B.A. Chin, H.A. Aglan, Y. Gan, Furnace brazing type 304 stainless steel to vanadium alloy (V-5Cr-5Ti), J. Nucl. Mater. 287 (2000) 1224–1228.

[13] M. Wu, L. Chang, L. Zhang, X. He, X. Qu, Effects of roughness on the wettability of high temperature wetting system, Surf. Coatings Technol. 287 (2016) 145–152.

[14] Granta, CES EduPack 2017, (2017).

[15] D. Shi, C. Dong, X. Yang, Y. Sun, J. Wang, J. Liu, Creep and fatigue lifetime analysis of directionally solidified superalloy and its brazed joints based on continuum damage mechanics at elevated temperature, Mater. Des. 45 (2013) 643–652.

[16] X. Chen, Z. Wang, D. Ding, H. Tang, L. Qiu, X. Luo, G. Shi, Strengthening and toughening strategies for tin bronze alloy through fabricating in-situ nanostructured grains, Mater. Des. 66 (2015) 60–66.

[17] K. Chen, X. Chen, D. Ding, G. Shi, Z. Wang, Crystallographic features of iron-rich nanoparticles in cast Cu-10Sn-2Zn-1.5Fe-0.5Co alloy, Mater. Charact. 113 (2016) 34–42.

[18] K. Chen, X. Chen, Z. Wang, H. Mao, R. Sandström, Optimization of deformation properties in as-cast copper by microstructural engineering. Part I. microstructure, J. Alloys Compd. 763 (2018) 592–605.

[19] S.R.B. Cooke, S. Aschenbrenner, The occurrence of metallic iron in ancient copper, J. F. Archaeol. 2 (1975) 251–266.

[20] D.M. Minić, A. Gavrilović, D.M. Minić, L.D. Rafailović, P. Angerer, J. Wosik, A. Mariĉić, Phase transformations of Fe73.5Cu1Nb3Si15.5B7amorphous alloy upon thermal treatment, J. Alloys Compd. 504 (2010) 462–467.

[21] X. Shu, G. Chen, J. Liu, B. Zhang, J. Feng, Microstructure evolution of copper/steel gradient deposition prepared using electron beam freeform fabrication, Mater. Lett. 213 (2018) 374–377.

[22] S. Klein, S. Weber, W. Theisen, Effect of heat treatment on phase structure and thermal conductivity of a copper-infiltrated steel, J. Mater. Sci. 50 (2015) 3586–3596.

[23] A. Chbihi, X. Sauvage, D. Blavette, Atomic scale investigation of Cr precipitation in copper, Acta Mater. 60 (2012) 4575–4585.

[24] A. Popovich, V. Sufiiarov, I. Polozov, E. Borisov, D. Masaylo, A. Orlov, Microstructure and mechanical properties of additive manufactured copper alloy, Mater. Lett. 179 (2016) 38–41.

[25] P.G. Sanders, J.A. Eastman, J.R. Weertman, Elastic and tensile behavior of nanocrystalline copper and palladium, Acta Mater. 45 (1997) 4019–4025.

[26] X. Zhang, C. Lin, S. Cui, Z. Li, Characteristics of nano-alumina particles dispersion strengthened copper fabricated by reaction synthesis, Rare Met. Mater. Eng. 45 (2016) 893–896.
[27] Y. Suezawa, Relation between the mechanical properties of the steel brazed joints and its filler metal elements and surface roughness of base metal, in: Proc. 23rd Heat Treat. Soc. Conf., 2006: pp. 135–142.
[28] P. Paris, F. Erdogan, A critical analysis of crack propagation laws, J. Basic Eng. 85 (1963) 528–533.
[29] J. Günther, D. Krewerth, T. Lippmann, S. Leuders, T. Tröster, A. Weidner, H. Biermann, T. Niendorf, Fatigue life of additively manufactured Ti–6Al–4V in the very high cycle fatigue regime, Int. J. Fatigue. 94 (2017) 236–245.
[30] A.M.P. De Jesus, R. Matos, B.F.C. Fontoura, C. Rebelo, L. Simões Da Silva, M. Veljkovic, A comparison of the fatigue behavior between S355 and S690 steel grades, J. Constr. Steel Res. 79 (2012) 140–150.
[31] R. Seifi, R. Hosseini, Experimental study of fatigue crack growth in raw and annealed pure copper with considering cyclic plastic effects, Theor. Appl. Fract. Mech. 94 (2018) 1–9.
[32] K. Obrtlík, J. Polák, M. Hájek, A. Vašek, Short fatigue crack behaviour in 316L stainless steel, Int. J. Fatigue. 19 (1997) 471–475.
[33] J. Newman Jr, The merging of fatigue and fracture mechanics concepts: a historical perspective, Prog. Aerosp. Sci. 34 (1998) 347–390.
[34] C.W. BROWN, M.A. HICKS, a Study of Short Fatigue Crack Growth Behaviour in Titanium Alloy ImI 685, Fatigue Eng. Mater. Struct. 6 (1983) 67–76.

List of figures

Figure 9: Fracture surfaces of (a) defect-free and (b) defect-bearing joints; (c) enlarged view of (a) fatigue crack initiated from the sample surface; (d) enlarged view of (b) fatigue crack initiated from the joint defect. Both samples are from batch 7 (OPS)

Figure 10: (a) Defect region and texture patterns within the fatigue crack initiation zone (batch 7); EDS elemental mapping of (b) chromium Cr; (c) iron Fe and (d) copper Cu of the selected rectangular region in (a)

Figure 11: Fatigue striation spacings at the early-stage fatigue crack propagation regions of defect-bearing samples with an initial defect area of (a) A=0.03 mm^2, batch 7A; (b) A=0.05 mm^2, batch 6A; (c) A=0.17 mm^2, batch 3A; (d) A=0.60 mm^2, batch 7B; and (e) A=1.47 mm^2, batch 6B. Batch ID A & B represents two individual specimens that have the same interface roughness conditions

Figure 12: Longitudinal sections of the fatigue fractured samples, (a) from batch 1 (P80), (b) from batch 2 (P180) and (c) from batch 7 (OPS)

Figure 13: Fracture surface of a specimen from batch 2 (P180) showing the defect, fatigue crack propagation and final fracture zones; the insets illustrate fatigue samples where cracks initiated from either a large or a small defect.

Figure 14: Relationship between the joint defect area and the corresponding fatigue life for all the fatigue tests performed at σ_a=180 MPa; the insets show the relationship between joint defect area and fatigue life, and the initial fatigue crack growth rate as a function of ΔK on logarithmic scales